

Notch filtering the nuclear environment of a spin qubit

Filip K. Malinowski[†], Frederico Martins[†], Peter D. Nissen¹, Edwin Barnes^{2,3}, Łukasz Cywiński⁴, Mark S. Rudner^{1,5}, Saeed Fallahi⁶, Geoffrey C. Gardner^{6,7}, Michael J. Manfra^{6,7}, Charles M. Marcus¹ and Ferdinand Kuemmeth^{1*}

Electron spins in gate-defined quantum dots provide a promising platform for quantum computation^{1–7}. In particular, spin-based quantum computing in gallium arsenide takes advantage of the high quality of semiconducting materials, reliability in fabricating arrays of quantum dots and accurate qubit operations^{5–10}. However, the effective magnetic noise arising from the hyperfine interaction with uncontrolled nuclear spins in the host lattice constitutes a major source of decoherence^{4,5,10,11}. Low-frequency nuclear noise, responsible for fast (10 ns) inhomogeneous dephasing⁵, can be removed by echo techniques^{4,5,11–14}. High-frequency nuclear noise, recently studied via echo revivals^{4,11}, occurs in narrow-frequency bands related to differences in Larmor precession of the three isotopes ⁶⁹Ga, ⁷¹Ga and ⁷⁵As (refs 15–17). Here, we show that both low- and high-frequency nuclear noise can be filtered by appropriate dynamical decoupling sequences, resulting in a substantial enhancement of spin qubit coherence times. Using nuclear notch filtering, we demonstrate a spin coherence time (T_2) of 0.87 ms, five orders of magnitude longer than typical exchange gate times, and exceeding the longest coherence times reported to date in Si/SiGe gate-defined quantum dots^{18,19}.

The qubit under study is implemented in a gate-defined double dot, with a potential that can be manipulated via nanosecond voltage pulses applied to gate electrodes V_L , V_M and V_R (Fig. 1a and Methods). The qubit states are encoded in the two-electron spin singlet state, $|S\rangle = (1/\sqrt{2})(|\uparrow\downarrow\rangle - |\downarrow\uparrow\rangle)$, and the spin triplet state, $|T_0\rangle = (1/\sqrt{2})(|\uparrow\uparrow\rangle + |\downarrow\downarrow\rangle)$, where the arrows indicate the spin projections of the electrons in the left and right dots, respectively^{5,8}. These qubit states are energetically separated from the spin-polarized two-electron states, $|\uparrow\uparrow\rangle$ and $|\downarrow\downarrow\rangle$, by an external magnetic field B^{ext} , ranging from 0.2 to 1 T in this experiment. Single-shot readout of the qubit is accomplished using spin-to-charge conversion followed by readout of a proximal sensor dot^{13,20} (see Methods).

As illustrated in Fig. 1b,d, the local Zeeman energy in dot $d = L, R$ is perturbed by the Overhauser field B_d^{nuc} arising from the hyperfine interaction with the nuclear spin bath. In our device, each electron is in contact with $\sim 10^6$ nuclear spins, comprised of three species: ⁶⁹Ga, ⁷¹Ga and ⁷⁵As (refs 4,5,17).

The Bloch sphere of the S– T_0 qubit is shown in Fig. 1c. Bold arrows indicate the rotation axes associated with the exchange interaction, J , and the gradient of the effective field between the dots, $\Delta B^{\text{tot}} = B_L^{\text{tot}} - B_R^{\text{tot}}$, where $B_d^{\text{tot}} = \sqrt{|B^{\text{ext}} + B_d^{\text{nuc}}|^2}$ is the magnitude of

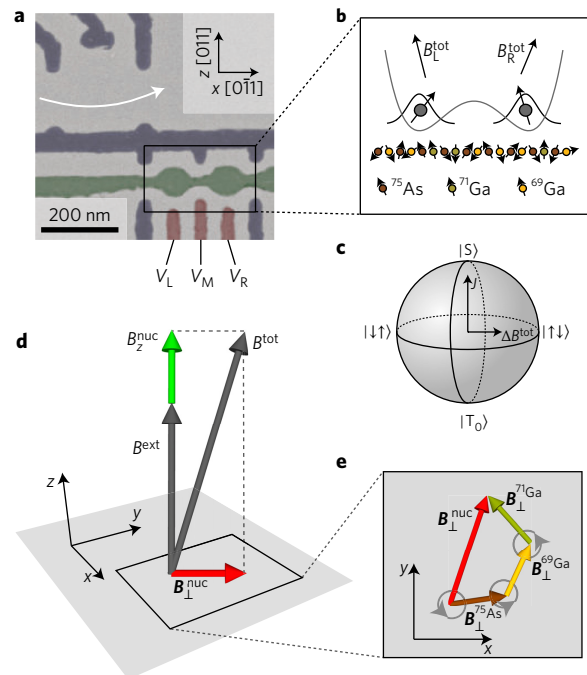


Figure 1 | Singlet-triplet qubit interacting with a nuclear spin bath.

a, False-colour scanning electron micrograph of a device similar to the one measured, consisting of a double dot (black rectangle) and a proximal readout dot (indicated by white arrow). The charge state and tunnel coupling of the double dot can be controlled on a nanosecond timescale by applying voltage pulses to gates V_L , V_M and V_R . **b**, Double-well potential occupied by two electrons (region indicated with black rectangle in **a**). Within the left (right) dot an effective magnetic field $B_{L(R)}^{\text{tot}}$ splits the electron spin states due to the Zeeman effect and hyperfine interaction with spinful nuclei of ⁶⁹Ga, ⁷¹Ga and ⁷⁵As. **c**, Bloch sphere representation of the qubit with corresponding two-electron spin states indicated. Two rotation axes are defined by the exchange interaction, J , and the total field gradient between the dots, $\Delta B^{\text{tot}} = B_L^{\text{tot}} - B_R^{\text{tot}}$. **d**, The effective magnetic field B^{tot} acting on each spin is set by the external magnetic field B^{ext} (nominally aligned with the [011] crystal axis), the slowly fluctuating Overhauser field component B^{nuc} parallel to B^{ext} , and the rapidly changing transverse Overhauser field B_{\perp}^{nuc} . **e**, The transverse Overhauser field $B_{\perp}^{\text{nuc}} = B_{\perp}^{\text{69Ga}} + B_{\perp}^{\text{71Ga}} + B_{\perp}^{\text{75As}}$ is a sum of fields of the three nuclear species, each precessing at its Larmor frequency.

¹Center for Quantum Devices and Station Q Copenhagen, Niels Bohr Institute, University of Copenhagen, Copenhagen 2100, Denmark. ²Department of Physics, Virginia Tech, Blacksburg, Virginia 24061, USA. ³Condensed Matter Theory Center and Joint Quantum Institute, Department of Physics, University of Maryland, College Park, Maryland 20742-4111, USA. ⁴Institute of Physics, Polish Academy of Sciences, Aleja Lotnikow 32/46, PL-02668 Warsaw, Poland. ⁵Niels Bohr International Academy, Niels Bohr Institute, Copenhagen 2100, Denmark. ⁶Department of Physics and Astronomy, Birkbeck Nanotechnology Center, and Station Q Purdue, Purdue University, West Lafayette, Indiana 47907, USA. ⁷School of Materials Engineering, Purdue University, West Lafayette, Indiana 47907, USA. [†]These authors contributed equally to this work. *e-mail: kuemmeth@nbi.dk

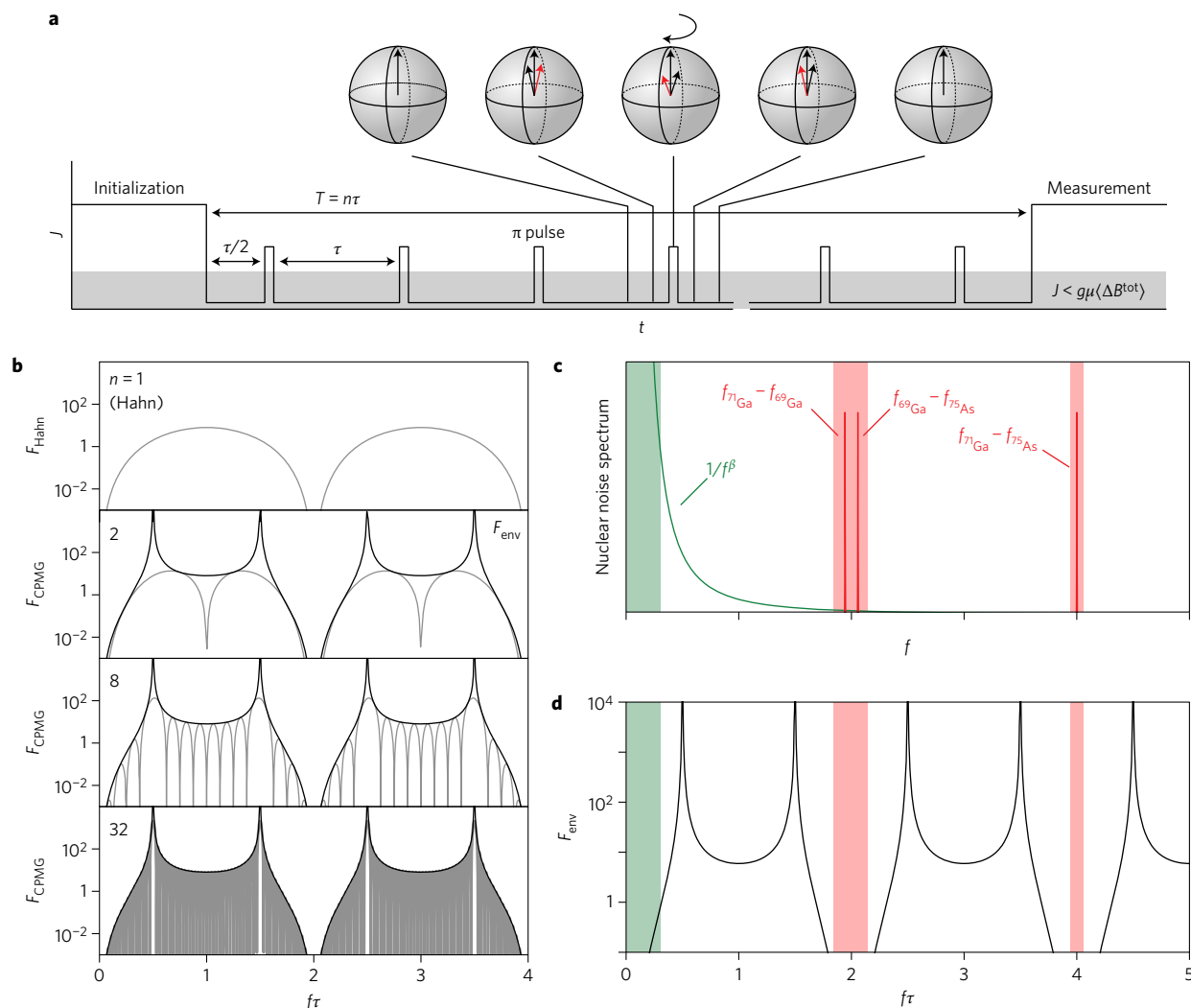


Figure 2 | Frequency-selective dynamical decoupling. **a**, CPMG pulse sequence consisting of n pulses separated by time τ . At the beginning, two electrons prepared in a singlet state $|S\rangle$ (initialization) are rapidly separated into two dots with exchange splitting $J < g\mu(\Delta B^{\text{tot}})$ (shaded region), where g is the g -factor in GaAs and μ is the Bohr magneton. After a total separation time $T = n\tau$, the preserved qubit state is detected by the readout dot via spin-to-charge conversion (measurement). During the separation time the two-electron state evolves in the fluctuating gradient of total magnetic field ΔB^{tot} . For slow fluctuations, the phases acquired before and after each π pulse cancel each other due to the sign reversal of the acquired phase by the π pulse. This is exemplified for three different values of ΔB^{tot} by arrows in the Bloch sphere. **b**, Filter functions of Hahn echo ($n = 1$) and CPMG sequences with $n = 2, 8$ and 32 π pulses (grey). Envelope of the filter function F_{env} reveals a frequency selectivity that is independent of n (black). **c**, Schematic spectral density of nuclear noise. The linear low-frequency part (green), described by a power law, is dominated by fluctuations associated with diffusion of the longitudinal component of the nuclear spin. The quadratic high-frequency noise (red) results from fluctuations of B^{tot} at differences of nuclear Larmor frequencies. **d**, By adjusting the time between π pulses, the minima of the filter function envelope F_{env} (black) can be aligned with the nuclear noise spectrum (green and red shading), thereby decoupling the qubit from both linear low-frequency and quadratic high-frequency noise.

the total effective field in dot d (ref. 8). Note that transverse nuclear field gradients tilt the quantization axes in the two dots relative to each other. For large external fields this primarily leads to a minor redefinition of the qubit subspace¹⁷; for simplicity we refer to the states in the qubit subspace with the conventional labels S and T_0 .

Overhauser field fluctuations in each dot are non-Markovian, with low-frequency (power-law) spectral content parallel to the external field, denoted B_z^{nuc} (suppressing the dot index), and narrowband spectral components at the nuclear Larmor frequency scale perpendicular to the external field, denoted B_{\perp}^{nuc} . Low-frequency fluctuations arise primarily from nuclear spin diffusion²¹, driven by dipole–dipole interactions between neighboring nuclei, and nonlocal electron-mediated flip-flops^{15,16,22,23}. High-frequency fluctuations of B_{\perp}^{nuc} arise primarily due to the megahertz-scale

relative Larmor precession of different nuclear spins^{4,11,17}. The transverse Overhauser field B_{\perp}^{nuc} is given by the sum of contributions $B_{\perp}^{69\text{Ga}}$, $B_{\perp}^{71\text{Ga}}$ and $B_{\perp}^{75\text{As}}$ of the three isotopic species, each of which precesses at its own Larmor frequency (Fig. 1e). This leads to modulations of the total field in each dot, B^{tot} , which are concentrated near the differences of the nuclear Larmor frequencies, and contribute quadratically to the qubit splitting.

To decouple the qubit from the multiscale nuclear noise, we employ the Carr–Purcell–Meiboom–Gill (CPMG) pulse sequence shown in Fig. 2a. We first initialize the double dot in a spin singlet by temporarily loading two electrons into the left dot. Then we quickly separate the electrons in the double-well potential, thereby rapidly turning off the exchange interaction, J . In this configuration, the gradient of the total effective field, ΔB^{tot} , causes uncontrolled qubit rotation around the horizontal axis of the

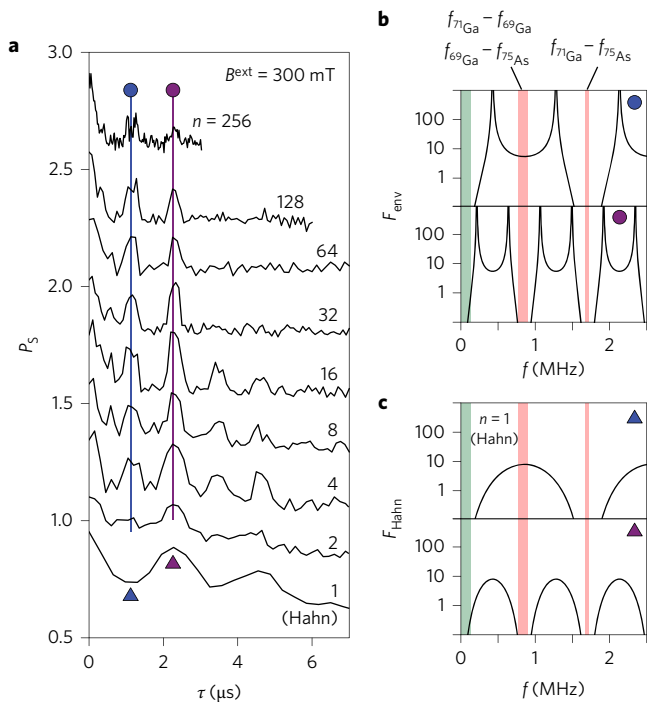


Figure 3 | Revival of coherence due to decoupling from nuclear Larmor precession. **a**, Singlet return probability, P_s , as a function of the time between π pulses, τ , for various numbers of π pulses, n . Curves are offset for clarity. Spheres and triangles indicate corresponding alignment of filter function relative to Larmor difference frequencies in **b** and **c**. **b**, Filter function envelope (black) and nuclear noise frequencies expected at 300 mT (shaded) for two choices of τ . In both cases (marked by blue and purple lines in **a**), the revival in P_s appears when minima of the filter function align with nuclear difference frequencies. **c**, Filter function of Hahn-echo sequence for the same choices of τ as in **b**. The absence of the first revival (marked by a blue triangle in **a**) indicates that coherence is lost when the maximum of the filter function overlaps with the peaks in the nuclear noise spectrum (shaded). The revival of P_s for the second choice of τ (marked by the purple triangle in **a**) corroborates the destructive role of nuclear Larmor dynamics in qubit decoherence.

Bloch sphere shown in Fig. 1c. After a time $\tau/2$, an exchange pulse is applied by temporarily lowering the barrier between dots with a voltage pulse on gate V_M (ref. 10), implementing a π rotation around the vertical axis of the Bloch sphere, followed by another waiting time $\tau/2$ (see Supplementary Section 1). We repeat this set of operations n times (where n is even) and, after a total evolution time $T = n\tau$, read-out the state of the qubit. The fraction of singlet outcomes is denoted P_s . Setting $n = 1$ implements a Hahn-echo sequence, and allows comparison with previous work^{4,11,24}.

For quasistatic nuclear noise, the effective field acting on the qubit before and after each π pulse is nearly the same, causing the qubit state to be refocused to the singlet state at the end of the sequence. For nuclear noise with power spectrum $S(f)$, Hahn and CPMG sequences act as a filter of the noise in the frequency domain (f)^{25–30}. For Gaussian noise, decoherence is described by a function

$$W(\tau) = \exp\left(-\int_0^\infty \frac{df}{2\pi^2} S(f) \frac{F(f\tau)}{f^2}\right) \quad (1)$$

corresponding to a singlet probability $P_s(\tau) = (1/2)[W(\tau) + 1]$. In this expression, $F(f\tau)$ is a filter function that depends on the particular pulse sequence.

Filter functions for Hahn echo (F_{Hahn}) and several CPMG sequences ($F_{\text{CPMG},n}$) for fixed τ are plotted in Fig. 2b (grey) for

varying numbers of π pulses. We write the CPMG filter function as a product $F_{\text{CPMG},n} = (1/2)F_{\text{FID}} \times F_{\text{env}}$, where F_{FID} is the filter function corresponding to the free induction decay and F_{env} is a slowly varying envelope (see Methods). F_{env} is periodic with period $2/\tau$, with minima occurring at zero frequency and multiples of $2/\tau$ (Fig. 2b, black), independent of n . Specific features of the filter functions can be exploited to decouple the qubit from its characteristic noise environment. First, for fixed separation time $T = n\tau$, the filter minimum near zero frequency becomes wider for increasing n (that is, decreasing τ ; note that the horizontal axis in Fig. 2b is normalized frequency $f\tau$). Thus for fixed T , decoupling from low-frequency $1/f^\beta$ -type noise ($\beta > 0$) becomes more efficient as n increases. Second, the minima that occur at multiples of $1/\tau$ indicate that noise at these frequencies is notch-filtered, in the sense that specific narrow-frequency windows are suppressed.

A schematic of the spectral density of nuclear noise for the S-T₀ qubit fabricated in a GaAs heterostructure is shown in Fig. 2c, distinguishing longitudinal low-frequency noise (green) and transverse narrowband noise (red). The low-frequency longitudinal contribution is well described by a power-law spectrum^{14,21}, and can be removed efficiently by any CPMG sequence (Fig. 2d). The high-frequency transverse contribution due to relative Larmor precession of nuclei is concentrated near the three Larmor frequency differences¹⁶, at megahertz frequencies for tesla-scale applied fields. Remarkably, two of the Larmor difference frequencies, $f_{71\text{Ga}} - f_{69\text{Ga}}$ and $f_{69\text{Ga}} - f_{75\text{As}}$, are nearly equal, independently of magnetic field, and hence the third frequency difference, $f_{71\text{Ga}} - f_{75\text{As}}$, occurs at twice that frequency. This coincidental property of the three nuclear species allows us to approximately align minima of the filter function with all three frequency differences by correctly choosing the time between π pulses, τ , thereby decoupling the qubit from low- and high-frequency nuclear noise simultaneously.

We now demonstrate the efficacy of this notch-filtering strategy in our experimental set-up. The narrowband character of the high-frequency nuclear noise is revealed by plotting the observed singlet return probability P_s as a function of time τ between π -pulses (rather than total separation time T). Independent of the choice of n , we observe an initial loss of coherence followed by revivals at $\tau \approx 1.1, 2.2, 3.3, \dots \mu\text{s}$ (Fig. 3a). These values of τ correspond to decoupling conditions shown in Fig. 3b, namely the alignment of nuclear difference frequencies (red) with minima of the filter function envelope. Qualitatively, the alternating depth of filter minima in Fig. 3b also explains the alternating heights of revivals, most pronounced for $n = 4$ in Fig. 3a. With increasing τ , the height of the revivals decreases. This is related to decoherence arising from low-frequency noise (shaded green in Fig. 3b)¹⁴. Revivals observed for Hahn-echo sequences can be explained similarly, except that the filter function for $\tau \approx 1.1 \mu\text{s}$ has a maximum near 0.9 MHz (Fig. 3c), rather than a minimum. Accordingly, P_s shows a minimum near $\tau = 1.1 \mu\text{s}$ instead of a revival (see $n = 1$ data in Fig. 3a).

The dependence of the decoupling condition for τ on nuclear Larmor dynamics can be verified by changing the applied magnetic field. In Fig. 4a, we fix $n = 256$ and measure the decay of coherence as a function of B^{ext} . As expected for a linear nuclear Zeeman splitting we find that the positions of the revival peaks follow a $1/B^{\text{ext}}$ dependence. We further observe that the peaks in $P_s(\tau)$ disappear at low magnetic fields. This may arise from several effects. First, the transverse Overhauser field in each dot, B_1^{nuc} , affects the total electronic Zeeman energy more strongly at low magnetic field (Fig. 1d), thereby accelerating dephasing. Second, the energy mismatch between nuclear and electron Zeeman splittings becomes smaller at low fields, increasing electron-mediated interactions between nuclear spins and the associated low-frequency noise^{16,23,31}. Third, an increase in τ , as needed to maintain the decoupling condition at lower fields, narrows the filter function minima and thus reduces decoupling from high-frequency noise.

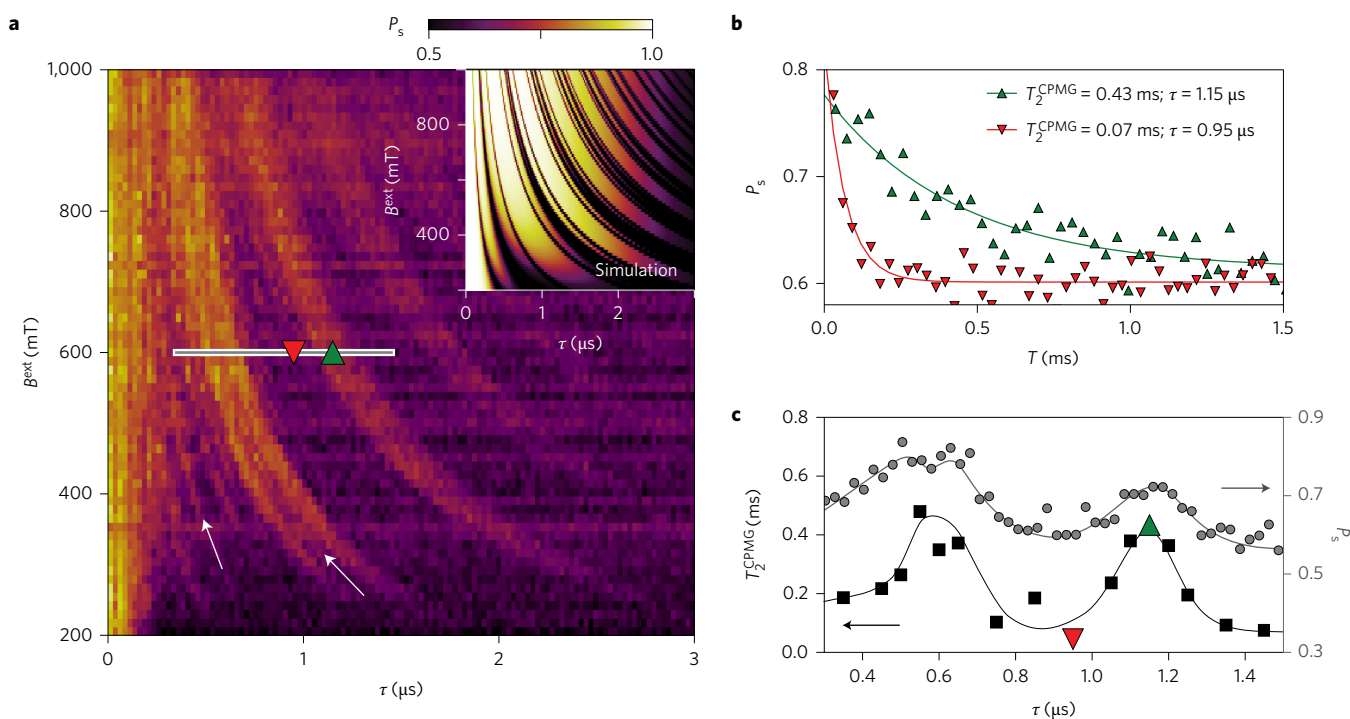


Figure 4 | Effect of magnetic field and τ on qubit coherence. **a**, Singlet return probability P_S as a function of time between π pulses, τ , and external magnetic field, B^{ext} , for a fixed number of π pulses, $n = 256$. Inset: a semiclassical model, generalizing the model of ref. 17 to the case of CPMG sequences, with no free parameters (see Supplementary Section 2). Arrows indicate fine features that the model fails to reproduce. **b**, Singlet return probability, P_S , measured as a function of total separation time $T = n\tau$, where n is varied between 32 and 1,536, for $\tau = 0.95$ and $1.15 \mu\text{s}$ at $B^{\text{ext}} = 600$ mT, the values marked in **a**. Solid lines are fits to a decay law with exponential decay time T_2^{CPMG} (see Methods). **c**, Coherence time T_2^{CPMG} , measured by increasing n as in **b**, as a function of τ (squares). For comparison, P_S for constant n , reproduced from the grey cut in **a**, is also shown (circles). Lines are guides to the eye. Triangles indicate the coherence times obtained from **b**.

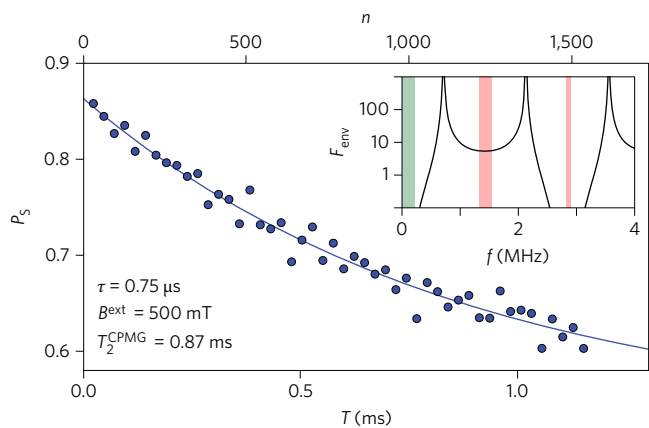


Figure 5 | Singlet return probability, P_S , as a function of total separation time, $T = n\tau$, for optimized and fixed values of τ and B^{ext} . An exponential fit to the data yields $T_2^{\text{CPMG}} = 0.87 \pm 0.13$ ms. The data points correspond to the CPMG sequences with $n = 32$ to $1,536\pi$ pulses. Inset: alignment of the filter function envelope (black) with nuclear noise spectrum (shaded) for this choice of τ and B^{ext} . Shaded regions indicate frequency range of nuclear noise.

Next, we show that revivals in P_S translate to prolonged qubit coherence times, by increasing n while keeping τ and B^{ext} fixed. This method, pioneered in NMR³², differs from other spin qubit experiments in which n is held constant while τ is swept proportionally to T (refs 4,14). Figure 4b plots decay curves $P_S(T = n\tau)$ obtained for $\tau = 0.95$ and $1.15 \mu\text{s}$ at $B^{\text{ext}} = 600$ mT (the corresponding points are indicated in Fig. 4a). For large n and Gaussian noise, an exponential decay of coherence is expected, independent of the power spectrum of the noise³⁰. By fitting exponential decay curves^{30,32} (see Methods),

we extract drastically different coherence times T_2^{CPMG} , as indicated. Values of T_2^{CPMG} for more choices of τ are plotted in Fig. 4c, along with $P_S(\tau)$ extracted from Fig. 4a. We observe a clear correlation between T_2^{CPMG} and $P_S(\tau)$, indicating that qubit coherence is significantly prolonged whenever the decoupling condition is fulfilled. The exponential decay indicates that coherence is limited by either incompletely filtered longitudinal noise or pulse errors.

Finally we comment on the limits of preserving qubit coherence. Most of the observed features in Fig. 4a are captured by a generalization of the semiclassical model of ref. 17, modified to include the details of the CPMG pulse sequence. The model involves four device-specific parameters (Fig. 4 inset): the effective number of nuclei interacting with each electron, $N = 7 \times 10^5$, a phenomenological broadening, $\delta B = 1.1$ mT, of the effective magnetic field acting on nuclei (likely due to quadrupolar splitting arising from electric-field gradients^{4,11,17}), the spectral diffusion time, $T_{\text{SD}} = 600 \mu\text{s}$, and the exponent associated with the linear low-frequency noise, $\beta = 3$ (all determined by independent measurements as described in Supplementary Sections 3 and 4). The model suggests that the longest coherence time may be achieved at high magnetic field (consistent with a reduced contribution of B_{\perp}^{nuc} to B^{tot} in each dot, see Fig. 1d), and for a decoupling condition corresponding to the second revival peak (Fig. 2d). We note that the model does not take pulse errors into account and does not show several fine features observed in experiment (see white arrows in Fig. 4a and Supplementary Section 5).

By exploring the parameter space between $B^{\text{ext}} = 300$ and $1,000$ mT with τ corresponding to the first revival peak, we observe coherence times around 0.7 ms for $B^{\text{ext}} = 500$ – 600 mT, with the largest being $T_2^{\text{CPMG}} = 0.87 \pm 0.13$ ms (Fig. 5), measured at $B^{\text{ext}} = 500$ mT and $\tau = 0.75 \mu\text{s}$. However, the number of examined values of B^{ext} and τ remains insufficient to resolve the fine structure apparent in the first revival peak.

We expect further improvements by using shorter π pulses and nuclear programming⁸. This will improve the fidelity of π pulses and suppress low-frequency noise, allowing the advantageous use of the decoupling condition in Fig. 2d at high magnetic fields and high pulse rates.

In summary, dynamical decoupling sequences were demonstrated to provide decoupling from narrowband high-frequency noise, acting as a notch filter for the nuclear environment. This technique was used to efficiently decouple a GaAs-based S-T₀ qubit from its nuclear environment. By synchronizing the repetition rate of π pulses in CPMG sequences with differences of nuclear Larmor frequencies, the coherence time of a S-T₀ qubit coupled to nuclear spin bath was extended to the millisecond regime (0.87 ms), five orders of magnitude longer than the gate operation time.

Methods

Methods and any associated references are available in the [online version of the paper](#).

Received 25 January 2016; accepted 12 August 2016;
published online 3 October 2016; corrected online 26 October 2016

References

- Loss, D. & DiVincenzo, D. P. Quantum computation with quantum dots. *Phys. Rev. A* **57**, 120–126 (1998).
- Veldhorst, M. *et al.* A two-qubit logic gate in silicon. *Nature* **526**, 410–414 (2015).
- Nowack, K. C. *et al.* Single-shot correlations and two-qubit gate of solid-state spins. *Science* **333**, 1269–1272 (2011).
- Bluhm, H. *et al.* Dephasing time of GaAs electron-spin qubits coupled to a nuclear bath exceeding 200 μ s. *Nat. Phys.* **7**, 109–113 (2011).
- Petta, J. *et al.* Coherent manipulation of coupled electron spins in semiconductor quantum dots. *Science* **309**, 2180–2184 (2005).
- Nowack, K. C., Koppens, F. H. L., Nazarov, Y. V. & Vandersypen, L. M. K. Coherent control of a single electron spin with electric fields. *Science* **318**, 1430–1433 (2007).
- Maune, B. M. *et al.* Coherent singlet-triplet oscillations in a silicon-based double quantum dot. *Nature* **481**, 344–347 (2012).
- Foletti, S., Bluhm, H., Mahalu, D., Umansky, V. & Yacoby, A. Universal quantum control of two-electron spin quantum bits using dynamic nuclear polarization. *Nat. Phys.* **5**, 903–908 (2010).
- Dial, O. E. *et al.* Charge noise spectroscopy using coherent exchange oscillations in a singlet-triplet qubit. *Phys. Rev. Lett.* **110**, 146804 (2013).
- Martins, F. *et al.* Noise suppression using symmetric exchange gates in spin qubits. *Phys. Rev. Lett.* **116**, 116801 (2016).
- Botzem, T. *et al.* Quadrupolar and anisotropy effects on dephasing in two-electron spin qubits in GaAs. *Nat. Commun.* **7**, 11170 (2016).
- Viola, L. & Lloyd, S. Dynamical suppression of decoherence in two-state quantum systems. *Phys. Rev. A* **58**, 2733–2744 (1998).
- Barthel, C., Medford, J., Marcus, C. M., Hanson, M. P. & Gossard, A. C. Interlaced dynamical decoupling and coherent operation of a singlet-triplet qubit. *Phys. Rev. Lett.* **105**, 266808 (2010).
- Medford, J. *et al.* Scaling of dynamical decoupling for spin qubits. *Phys. Rev. Lett.* **108**, 086802 (2012).
- Cywiński, L., Witzel, W. M. & Das Sarma, S. Electron spin dephasing due to hyperfine interactions with a nuclear spin bath. *Phys. Rev. Lett.* **102**, 057601 (2009).
- Cywiński, L., Witzel, W. M. & Das Sarma, S. Pure quantum dephasing of a solid-state electron spin qubit in a large nuclear spin bath coupled by long-range hyperfine-mediated interactions. *Phys. Rev. B* **79**, 245314 (2009).
- Neder, I. *et al.* Semiclassical model for the dephasing of a two-electron spin qubit coupled to a coherently evolving nuclear spin bath. *Phys. Rev. B* **84**, 035441 (2011).
- Eng, K. *et al.* Isotopically enhanced triple-quantum-dot qubit. *Sci. Adv.* **1**, e1500214 (2015).
- Kawakami, E. *et al.* Gate fidelity and coherence of an electron spin in a Si/SiGe quantum dot with micromagnet. Preprint at <http://arXiv.org/abs/1602.08334> (2016).
- Barthel, C., Reilly, D. J., Marcus, C. M., Hanson, M. P. & Gossard, A. C. Rapid single-shot measurement of a singlet-triplet qubit. *Phys. Rev. Lett.* **103**, 160503 (2009).
- Reilly, D. J. *et al.* Measurement of temporal correlations of the overhauser field in a double quantum dot. *Phys. Rev. Lett.* **101**, 236803 (2008).
- de Sousa, R. & Das Sarma, S. Theory of nuclear-induced spectral diffusion: spin decoherence of phosphorus donors in Si and GaAs quantum dots. *Phys. Rev. B* **68**, 115322 (2003).
- Yao, W., Liu, R. B. & Sham, L. J. Theory of electron spin decoherence by interacting nuclear spins in a quantum dot. *Phys. Rev. B* **74**, 195301 (2006).
- Childress, L. I. *et al.* Coherent dynamics of coupled electron and nuclear spin qubits in diamond. *Science* **314**, 281–285 (2006).
- Martinić, J., Nam, S., Aumentado, J., Lang, K. & Urbina, C. Decoherence of a superconducting qubit due to bias noise. *Phys. Rev. B* **67**, 094510 (2003).
- Cywiński, L., Lutchyn, R. M., Nave, C. P. & Das Sarma, S. How to enhance dephasing time in superconducting qubits. *Phys. Rev. B* **77**, 174509 (2008).
- Biercuk, M. J., Doherty, A. C. & Uys, H. Dynamical decoupling sequence construction as a filter-design problem. *J. Phys. B* **44**, 154002 (2010).
- Soare, A. *et al.* Experimental noise filtering by quantum control. *Nat. Phys.* **10**, 825–829 (2014).
- Kabytayev, C. *et al.* Robustness of composite pulses to time-dependent control noise. *Phys. Rev. A* **90**, 012316 (2014).
- Álvarez, G. A. & Suter, D. Measuring the spectrum of colored noise by dynamical decoupling. *Phys. Rev. Lett.* **107**, 230501 (2011).
- Deng, C. & Hu, X. Analytical solution of electron spin decoherence through hyperfine interaction in a quantum dot. *Phys. Rev. B* **73**, 241303(R) (2006).
- Carr, H. Y. & Purcell, E. M. Effects of diffusion on free precession in nuclear magnetic resonance experiments. *Phys. Rev.* **94**, 630–638 (1954).

Acknowledgements

We thank R. Eriksen for help in preparation of the reflectometry set-up. This work was supported by IARPA Multi-Qubit Coherent Operations (MQCO) programme, LPS-MPO-CMTC, the Polish National Science Centre (NCN) under grant no. DEC-2012/07/B/ST3/03616, the Army Research Office, the Villum Foundation and the Danish National Research Foundation.

Author contributions

S.F., G.C.G. and M.J.M. grew the heterostructure. P.D.N. fabricated the device. F.M., P.D.N., F.K. and F.K.M. prepared the experimental set-up. F.K.M., F.M. and F.K. performed the experiment. E.B., L.C. and M.S.R. developed the theoretical model and performed simulations. F.K.M., F.K., F.M., E.B., L.C., M.S.R. and C.M.M. analysed data and prepared the manuscript.

Additional information

Supplementary information is available in the [online version of the paper](#). Reprints and permissions information is available online at www.nature.com/reprints. Correspondence and requests for materials should be addressed to F.K.

Competing financial interests

The authors declare no competing financial interests.

Methods

The sample. The sample, identical to the one shown in Fig. 1a, is fabricated from a GaAs/AlGaAs quantum well grown by molecular beam epitaxy. Crystallographic axes are shown in Fig. 1a. A high-mobility 2D electron gas (2DEG) is formed 57 nm below the sample surface with carrier density $n_s = 2.5 \times 10^{15} \text{ m}^{-2}$ and mobility $\mu = 230 \text{ m}^2 \text{ V}^{-1} \text{ s}^{-1}$. Metallic gates, separated from the heterostructure by a 10-nm layer of HfO_2 , are used to confine two electrons in the region indicated by a rectangle in Fig. 1a. Gates indicated in blue and red are operated at negative voltages to deplete the 2DEG underneath, while gates coloured in green are biased with positive voltages to accumulate electrons underneath. The charge state and tunnel coupling of the double dot can be controlled on a nanosecond timescale by applying voltage pulses to gates V_L , V_M and V_R .

Initialization and readout of the qubit. The sample is measured at a base temperature of 25 mK in a cryofree dilution refrigerator, with an external magnetic field B^{ext} applied parallel to the z direction indicated in Fig. 1a. The qubit is initialized in a singlet state by tilting its charge state into the (2,0) charge configuration and allowing the exchange of electrons with the left lead near the (1,0) charge transition⁵.

After qubit manipulation the state of the qubit is measured by tilting the double well potential to favour the (2,0) charge state. If the two electrons are in the spin triplet configuration, Pauli blockade prevents reaching the (2,0) state, and the charge configuration remains (1,1). The charge state of the double dot modifies the conductance through a proximity sensor dot operated as a single-electron transistor. This sensor dot is embedded in a radiofrequency resonant circuit, enabling us to distinguish singlet and triplet states in 8 μs with a readout visibility of approximately 80%, as defined in ref. 13.

Envelope of a filter function for CPMG sequences. Filter functions for Hahn echo and CPMG sequences (for even number of π pulses, n) are given by²⁶

$$F_{\text{Hahn}}(f\tau) = 8 \sin^4\left(\frac{\pi f \tau}{2}\right) \tag{2}$$

$$F_{\text{CPMG},n}(f\tau) = \frac{8 \sin^4(\pi f \tau/2) \sin^2(\pi f \tau n)}{\cos^2(\pi f \tau)} \tag{3}$$

To emphasize the qualitative difference between CPMG sequences and the Hahn echo sequence, and represent features of CPMG filter functions relevant for large number of π pulses, n , we rewrite

$$F_{\text{CPMG},n} = \frac{1}{2} F_{\text{env}} \times F_{\text{FID}} \tag{4}$$

using n -independent filter function envelope

$$F_{\text{env}}(f\tau) = \frac{8 \sin^4(\pi f \tau/2)}{\cos^2(\pi f \tau)} \tag{5}$$

obtained by dividing $F_{\text{CPMG},n}$ by the filter function corresponding to free induction decay

$$F_{\text{FID}}(fT) = 2 \sin^2(\pi f T) \tag{6}$$

Here $T = n\tau$ corresponds to a free induction decay time equal to the total duration as a CPMG sequence. This normalization removes a fine comb related to the total length of the sequence.

Exponential fits to $P_S(T)$. In contrast to many spin qubit experiments^{4,5,9,11,13-16,19,22-24} we measure coherence not by keeping n constant and sweeping τ , but by increasing n while keeping τ constant. This method, which is standard in NMR experiments³², results in an exponential decay of coherence for a large number of π pulses, n , and long evolution times $T = n\tau$, independent of the power spectrum of the Gaussian noise³⁰. The rate of such a decay is determined by the noise spectrum at a frequency corresponding to the first peak of the filter function from Fig. 2d at $f = 1/2\tau$.

Therefore, we perform an exponential fit of the form $A + B \exp(-T/T_2^{\text{CPMG}})$ to the data, where A and B account for preparation and readout fidelity as well as rapid initial decay of the signal^{4,11}, and T_2^{CPMG} is the coherence time of the qubit. Typical values of A and B obtained from fits used to extract values of T_2^{CPMG} , shown in Fig. 4c, are $A \sim 0.6$ and $B \sim 0.2$. Fit to the data presented in Fig. 5 yields $A = 0.53$ and $B = 0.34$.